

Impact of aerosols and clouds on surface and
boundary layer dynamics over Southern
China: a 10-year trend analysis based on
reanalysis data

Student: Laura Izzo

Supervisors from KNMI: Nikos Benas and Jan Fokke Meirink
Supervisor from Wageningen UR: Jordi Vilà-Guerau de Arellano

April 23, 2018

Contents

1	Introduction and Background	4
1.1	Research aim and case study	5
2	Methodology	6
2.1	Dataset: CAMS interim reanalysis (CAMSiRA)	6
2.1.1	Surface variables	7
2.1.2	Model levels variables	8
2.2	Analysis	8
2.2.1	Yearly analysis	9
2.2.2	Monthly analysis	10
2.2.3	Diurnal analysis	10
2.2.4	Conditional Analysis	10
3	Results	11
3.1	Yearly analysis	11
3.1.1	Inland/coastal comparison	14
3.2	Monthly analysis	17
3.3	Diurnal analysis	17
3.3.1	Radiation budget analysis	18
3.3.2	Surface energy balance analysis	20
3.3.3	Potential temperature and specific humidity	21
4	Summary and Discussion	24
A	Model levels (CAMSiRA)	30
B	AOD components: spatial changes and correlation with LCC	31
C	Changes in AOD and LCC for all months	33
D	Vertical profiles	36
D.1	Potential temperature	36
D.2	Specific humidity	37

Abstract

This study characterizes the modifications in radiation, surface properties and atmospheric boundary layer (ABL) dynamics over Southern China in the 10-year period 2006-2015, under conditions of increasing cloud cover (CC) and decreasing aerosol optical depth (AOD), while supporting recent remote sensing evidence of these changes. Our analysis is carried out based on the atmospheric composition dataset CAMSiRA (Copernicus Atmosphere Monitoring Service interim Reanalysis), that is coupled to a meteorological model. To prove the validity of our approach, we compare the AOD and CC information given by CAMSiRA with those measured by MODIS (MODerate resolution Imaging Spectroradiometer). Firstly, the analysis is carried out on a yearly scale, analysing the changes in the variables in the 10-year period. We study the variability between a location in the inland and a location on the coast. Secondly, a monthly analysis is performed to determine in which month the largest changes of aerosols and clouds occur. Finally, a diurnal analysis characterizes the typical surface conditions for the month selected with the monthly analysis.

The comparison between the inland and coastal locations showed that changes are more pronounced over land than over sea. Over land, a decrease of 10.7% in short-wave incoming radiation (SW_{in}) occurs in the 10-year period under study. This seems connected with the large increase in cloud cover at this location (20%) which suggests a prevalence of cloudy-sky mechanisms over clear-sky mechanisms. The reduced SW_{in} leads to a lower amount of energy available in the system, causing a reduction in the sensible heat flux (H) and in the potential temperature (θ) in the ABL. Subsequently, the sensible heat flux is reduced and so is the height of the ABL.

1 Introduction and Background

Aerosols are small particles in suspension in the atmosphere that affect air quality, weather and climate through various mechanisms (Boucher, 2015). Their radius' dimension ranges from 1-10 μm (coarse particles) to 10^{-3} - 10^{-2} μm (ultra-fine aerosols) (Jacob, 1999). They are a class of air pollutants that is cause of great concern especially in the urban environment, because of its negative impacts on human health (Janhäll et al., 2006). In fact, the presence of aerosols in the lowest part of the atmosphere - the Atmospheric Boundary Layer (ABL) - is known to negatively affect human health, being associated with respiratory, cardiopulmonary and lung cancer mortalities (Anenberg et al., 2010).

The main direct consequences of the presence of aerosols on the atmospheric radiation budget are known as Aerosol-Radiation Interactions (ARI): these mainly consist of scattering and absorption of radiation (Boucher, 2015), through which aerosols affect Earth's climate by altering the radiation budget (Li et al., 2017; Jethva et al., 2016). Additionally, aerosols can affect cloud albedo and life time by means of Aerosol-Cloud Interactions (ACI). Finally, the interaction of aerosols with radiation can influence cloud properties, a mechanism termed semi-direct effect (SDE), which is grouped under the ARI. According to the SDE mechanism, absorbing aerosols at cloud level heat the cloud layer and enhance the cloud burn-off (Johnson et al., 2004).

The SDE is a cloudy sky mechanism and it consists of a reduction of low-cloud cover and liquid-water path (LWP) caused by aerosols absorbing solar radiation, which leads to positive radiative forcing (RF) (Johnson et al., 2004). Positive RF is indeed a potential consequence of absorbing aerosols, with varying intensity depending on aerosols' properties (Jethva et al., 2016) - such as scattering or absorption - and collocation with respect to the clouds (Koch and Del Genio, 2010).

By affecting the solar incoming radiation, aerosols affect the amount of energy available in the ABL and therefore surface fluxes, which influence the diurnal evolution of temperature in the ABL (Li et al., 2017). For example, aerosols reduce temperature and increase moisture, which leads to an increase in relative humidity (RH) and vice versa (Li et al., 2017). Indeed, it has been shown that aerosols can change the ABL height and characteristics of the entrainment zone (Barbaro et al., 2014). Clouds formation and properties are known to depend firstly on dynamical processes (Boucher, 2015), many of which originate in the ABL. Therefore, these alternative paths of indirect aerosol and cloud interactions, through changes in the ABL, are worth investigating.

To investigate these mechanism, a study by Benas et al. (2017) has been taken as a starting point. The next section describes the main findings of

that study and the aim of the present study.

1.1 Research aim and case study

Benas et al. (2017) recently investigated clouds and aerosols satellite observations from the MODerate resolution Imaging Spectroradiometer (MODIS) (Levy et al., 2013; Platnick et al., 2017) and the Satellite Application Facility on Climate Monitoring (CM SAF) CLOUD, Albedo and surface RADIATION data set – Edition 2 (CLARA-A2) during a 10-years period (2006-2015) on a global scale (Karlsson et al., 2017). What emerged from the observations was that particularly high changes in liquid water path (LWP) occurred over Southern China, an area extending in latitude between 20°N and 25°N and in longitude between 105°E and 115°E (Figure 1). The AOD change over the area in the same period was investigated, revealing a strong decrease (-17.6%).

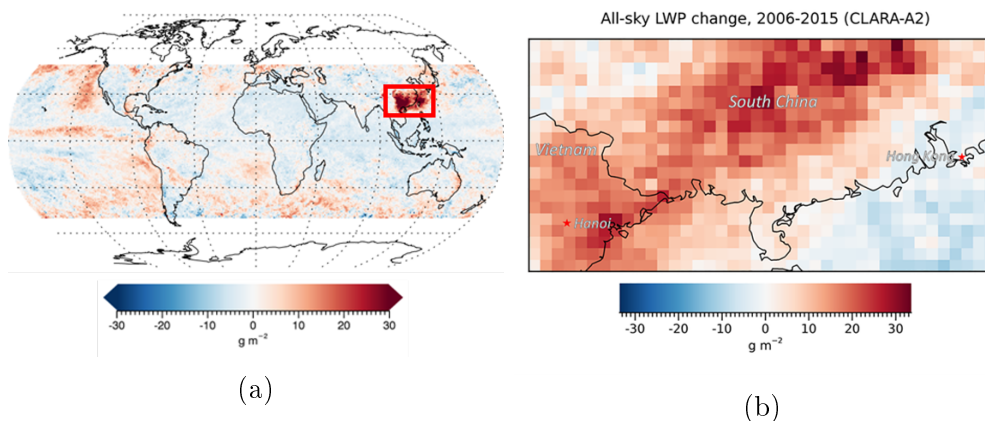


Figure 1: All-sky global liquid water path (LWP) changes in the period 2003-2015 from CLARA-A2 (a). The red box indicates the area where the highest changes in LWP were observed, which includes our study area (b). Courtesy of Benas et al. (2017)

Since in this case cloud cover and LWP increase under decreasing AOD, an indication of a possible reversed SDE mechanism is presented, meaning the mechanism manifested under decreasing absorbing aerosols. As shown in Figure 1.b, it is apparent that these changes are especially observed inland, since the LWP increase and AOD decrease have different magnitude of trends between the inland and the coastal area, being stronger over the inland.

The reduction in aerosols in that study was ascribed to human influence, specifically to the reduction in biomass burning aerosols occurred in the area during the 10-year period (Benas et al., 2017). The described changes were observed mainly in the late fall- early winter months. In particular, in these months cloud cover was enhanced the most when aerosol

changes happened within the cloud layer.

As mentioned in section 1, tropospheric aerosols interact with radiation and clouds. Surface fluxes respond to changes in SW_{in} and impact the evolution of the ABL dynamics.

Therefore, in this study our aim is to characterize the modifications of the radiation and surface properties, and their impact on surface and ABL dynamics for the studied area. The results of this study will serve as an input in a further modelling phase of this research, which will help gaining more insights into the role of aerosols in this case study.

Hence, the main research question of the present study is formulated as follows:

How do changes in clouds and aerosols affect radiation, surface properties and ABL dynamics over Southern China during the 10-year period 2006-2015?

2 Methodology

This research is based mainly on the CAMSiRA dataset, which is described in the first section of this chapter. It is a reanalysis dataset that combines satellite observations and modelling. In the second part of this chapter, the analysis strategy is defined.

2.1 Dataset: CAMS interim reanalysis (CAMSiRA)

The lack of extensive observational datasets is a major issue often encountered when studying the ABL, which is mainly due to the difficulties associated with observing the boundary layer from space (von Engel and Teixeira, 2013). Indeed, over the area of interest, insufficient surface and radio sounding observations are available at the needed time and space resolution. Therefore, this study is carried out based primarily on the CAMS (Copernicus Atmosphere Monitoring Service) (Flemming et al., 2017) reanalysis dataset from the European Centre for Medium Range Weather Forecast (ECMWF) for the period 2006-2015.

The CAMS interim reanalysis (CAMSiRA) is a global reanalysis dataset of atmospheric composition, coupled to meteorology, produced by CAMS (ECMWF, 2017b). It is currently the most complete atmospheric composition dataset available at the needed time frame. Indeed, it covers the period 2003-2015, with a spatial resolution of 110 km globally and a 3-hourly temporal resolution (output frequency) for forecast fields (ECMWF, 2017d). The assimilation system used is IFS Cycle 40r2 4D-Var. IFS is the Integrated Forecasting System and 4D-Var is a four dimensional variational data assimilation method that adjusts a short-range forecast (called the background) in space and time to bring it to closer agreement with

meteorological observations (ECMWF, 2017a). This means that it combines satellite observations with chemistry-aerosol modelling to produce a gridded continuous representation (analysis) of the mass mixing ratios of atmospheric trace gases and aerosols (Flemming et al., 2017). The source for biomass burning emissions is GFAS v. 1.2 (Global Fire Assimilation System). Data is produced at various levels (ECMWF, 2017c), of which we use the following two:

- *Surface fields*, which represent the meteorology near the surface, as well as a total column aggregation.
- *Model levels*, which are used in ECMWF’s forecast model to resolve the atmosphere in vertical. Here, they are used to study the vertical profiles of variables, since we are interested in the lower troposphere (more details can be found in Appendix). As an indication, around 10 levels out of 60 are found within the (diurnal) ABL.

2.1.1 Surface variables

Below is a summarized list of the surface variables from CAMSiRA used in this study.

- Components of the radiation budget [J m^{-2}].
- Components of the surface energy balance [J m^{-2}].
- ABL height [m].
- Total, low, medium and high cloud cover (0-1).¹
- 2 m temperature and dew point temperature [K].
- Total AOD at 550 nm, including AOD of five aerosol types (sea salt, dust, organic matter, black carbon, sulphate).

For our purpose, most of the variables can be analysed in the units provided. However, energy parameters are accumulated fields [J m^{-2}]. This means that every output value is an accumulated value since the start of the forecast, which is every 12 hours. The output is 3-hourly. Therefore, we calculated the average instantaneous value for the 3-hour period in W m^{-2} .

Net radiation (Q_{net}), upward fluxes (SW_{out} , LW_{out}) and ground heat flux

¹Low cloud cover: between surface and 0.8 of surface pressure; medium cloud cover: between 0.8 and 0.45 of surface pressure; high cloud cover: between 0.45 of surface pressure and the model top.

(G) are not available in the dataset, but are needed in order to have a complete radiation and surface energy budget. They are therefore calculated according to the following:

$$LW_{out} = LW_{net} - LW_{in} \quad (1)$$

$$SW_{out} = SW_{net} - SW_{in} \quad (2)$$

$$Q_{net} = LW_{in} - LW_{out} + SW_{in} - SW_{out} \quad (3)$$

$$G = Q_{net} - LE - H \quad (4)$$

Where LW_{out} is the long-wave (thermal) outgoing radiation, LW_{net} is the long-wave net radiation, LW_{in} is the long-wave incoming radiation, SW_{out} is the short-wave (solar) outgoing radiation, SW_{net} is the short-wave net radiation, SW_{in} is the short-wave incoming radiation, LE is the latent heat flux and H is the sensible heat flux. All radiation and surface energy components are in $W\ m^{-2}$. The equations take into account the signs of the radiation components.

2.1.2 Model levels variables

The model levels variables are used to recreate vertical profiles of the variables of interest. Logarithm of surface pressure, specific humidity [$kg\ kg^{-1}$] and air temperature [K] are available from the model output (See Appendix A for the calculation of the vertical gradient of pressure in CAMSiRA).

Since our aim is to study the ABL, we need to study conserved variables that are assumed to be homogeneous in the mixed layer. One of them is the specific humidity (q), already given by the output of CAMSiRA. The other one is the potential temperature (θ), defined as the temperature that an air parcel would have if it was brought adiabatically from its pressure to a standard pressure (usually 1000 hPa). The absolute temperature and the potential temperature are related by:

$$\theta = \left(T \frac{1000}{p}\right)^{R/c_p} \quad (5)$$

Which is possible for us to calculate, with T being the air temperature [K], p the pressure [hPa], $R/c_p = 0.287$ for air (where R is the gas constant of air, and c_p is the specific heat capacity at a constant pressure).

2.2 Analysis

Using the model data, we study the variations of the surface energy balance and ABL dynamics due to the aerosol and clouds presence.

As a first step, we compare AOD and liquid cloud fraction (LCF) from MODIS, used in the study by Benas et al. (2017) with the AOD and low

cloud cover (LCC) available from CAMSiRA. We chose to do so because liquid clouds are mainly located between the surface and ~ 800 hPa.

As described in section 1 (Introduction and Background), aerosols effects are divided into clear-sky and cloudy-sky mechanisms.

In clear-sky conditions, a reduction in absorbing aerosols will cause an increase in the SW_{in} , that should then lead to higher surface fluxes (Barbaro et al., 2014). Instead, SW_{in} is expected to be lower when (absorbing aerosol) AOD is higher. The decrease in SW_{in} should lead to reduced surface fluxes. These drive the diurnal evolution of the (thermo-)dynamics in the ABL. Therefore, these modifications are expected to affect ABL height, pollutants' concentration (Barbaro et al., 2014) and clouds formation.

Cloudy conditions would lead to different mechanisms, like the SDE, and result in different changes in SW_{in} than the above described ones. A distinction between a clear and a cloud day would be appropriate to get more insights into these processes, but it will be carried out in further research. In fact, for the SDE, lower AOD should lead to more clouds and thus lower SW_{in} and surface fluxes.

Given the spatial variation of trends in changes in AOD and LWP, a conditional analysis is set up, in which the changes in radiation, surface properties, ABL conditions are studied at different locations (an inland and a coastal one). Another conditional analysis compares different pollution conditions (more and less polluted years).

The variables described in the previous section are studied at three different scales: yearly, monthly and diurnal. We use the yearly analysis to identify changes in the whole 10-year period; the monthly analysis to compare changes among the various months; the diurnal analysis to study the diurnal variation of surface variables and ABL dynamics of a typical (average) day of a month selected with the monthly analysis. These three analysis scales are described in more detail in the next sections. The main analysis strategy consists of identification of trends, and calculation and comparison of statistical measures.

2.2.1 Yearly analysis

For every studied surface variable, the data of each of the 120 months (10 years x 12 months) are averaged to obtain one value per month. In this section the analysis consists mainly of time series of the resulting 120 monthly averages' time series, which allows to identify changes. The data in this section have been also studied after deseasonalization, according to:

$$x_{i,j}^d = x_{i,j} - \frac{1}{N_i} \sum_i x_{i,j} + \frac{1}{N_i N_j} \sum_i \sum_j x_{i,j} \quad (6)$$

Where $x_{i,j}^d$ is the deseasonalized value for each month, $x_{i,j}$ is the monthly average of the variable for each month (j) of each year (i), N_i is the number

of years and N_j is the number of months.

The deseasonalization allows the removal of the seasonal variation, highlighting variations due to other factors. Statistical values like percentage of changes, standard deviation and significance of the change are calculated and compared. In section 3 (Results), all percentage changes have been calculated on the linear fit of the deseasonalized time series, while standard deviation is calculated on non-deseasonalized values.

2.2.2 Monthly analysis

This analysis is meant to compare the changes among the various months, in order to identify the month to focus on for the diurnal cycle analysis. The criteria in selecting the month consisted in the most significant or highest correlated changes in AOD and cloud cover.

The analysis focuses on a late fall-early winter month (e.g. October-January), because in these months the strongest and highest correlated trends in aerosol and cloud properties were found by Benas et al. (2017). Besides, literature in general shows that winter months are particularly critical for air quality, due to wintertime haze days, temperature inversion episodes and human activities' temporal variation (Janhäll et al., 2006; Zhao et al., 2016; Yang et al., 2016).

2.2.3 Diurnal analysis

Both surface variables and model level variables are analysed on a diurnal scale. The aim of this analysis is to determine a characteristic diurnal evolution of the ABL in the studied area. The 'typical' day is an average of all days of the month selected in the monthly analysis. Eventually, 4 average days are defined and analysed:

- an average inland day of a more polluted year;
- an average inland day of a less polluted year;
- an average coastal day of a more polluted year;
- an average coastal day of a less polluted year.

This analysis is aimed to give an insight into the changes in ABL conditions due to spatial and temporal changes in AOD and cloud cover.

2.2.4 Conditional Analysis

The selected inland location should combine both large changes in cloud cover (increase) and in AOD (decrease). On the contrary, the selected

coastal location should combine low changes in cloud cover and AOD, in order to serve as a "control" (mostly stable) case. This selection is carried out after calculating the Pearson correlation coefficient (Pearson r) between AOD decrease and cloud cover increase. We choose the Pearson correlation coefficient because it is a measure of the linear correlation between two variables, which serves our purpose. It ranges between -1 and +1, where 1 is the total positive linear correlation, 0 is no linear correlation and -1 is total negative linear correlation.

At these two locations, a comparison between ABL conditions in more polluted and less polluted years is carried out.

3 Results

In this section, the results of the analysis of variables from the CAMSiRA dataset are presented. First, the results of the yearly analysis (3.1) are illustrated, along with a comparison of AOD and LCC from CAMSiRA and AOD and LCF from MODIS. The results from the monthly analysis (3.2) follow and, finally, the results of the diurnal analysis (3.3).

3.1 Yearly analysis

Firstly, the AOD and LCC from CAMSiRA have been compared to the AOD and LCF from MODIS.

For the AOD, CAMSiRA shows an average of 0.42 and a decrease of 13.5%, while MODIS shows an average AOD of 0.51 with a decrease of 17.7%. For LCC, CAMSiRA shows an average of 0.37 and an increase of 23.9%, while MODIS has an average LCF of 0.47 and an increase of 6.8%. For both variables CAMSiRA is almost always lower than MODIS and shows a smaller decrease for AOD but a larger increase in LCC. The two datasets show similar change and seasonal variation for both variables. The 10-years period monthly means of AOD and LCC/LCF from CAMSiRA and MODIS, averaged over the whole study area, are found in Figure 2.

In CAMSiRA the AOD components are classified as in 2.1 (Surface variables). The contribution of each of these components to the total AOD is analysed and the results reveal that sulphate aerosols happen to be the main contributor, with an AOD of 0.25. Organic matter aerosols follow with an AOD of 0.12, black carbon and dust aerosols are both 0.03 and sea salt aerosols are contributing the least with 0.01 (Figure 3).

The similarities in AOD changes and LCC/LCF changes between CAMSiRA and MODIS allow us to proceed with the analysis of the surface vari-

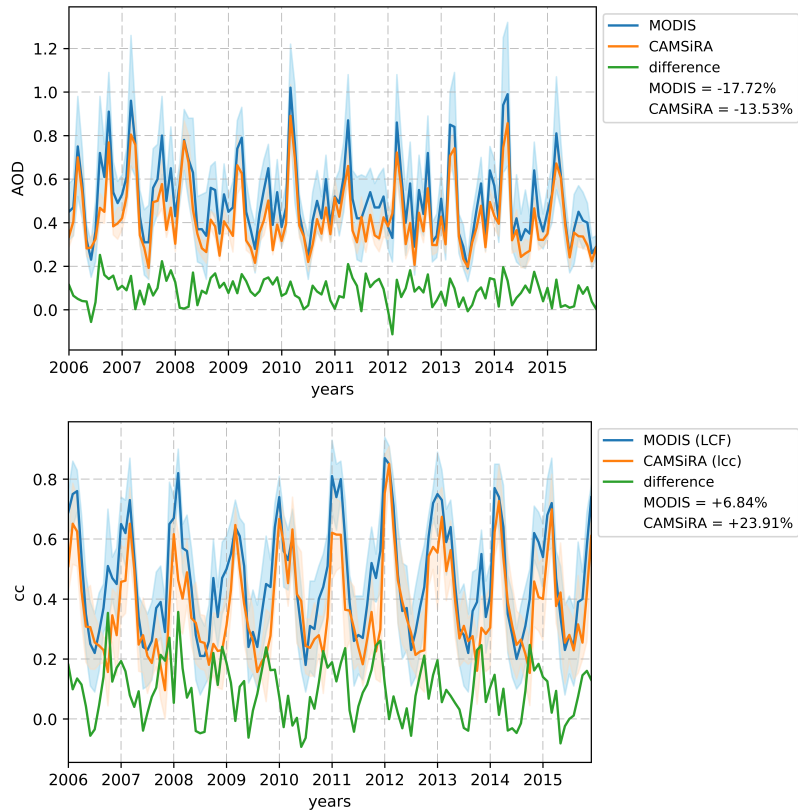


Figure 2: Top: 10-years time series of AOD monthly means from MODIS and CAMSiRA, averaged over the whole study area. Changes are significant both for MODIS (pvalue = 0.002) and CAMSiRA (pvalue = 0.013). Bottom: same, but for LCF (from MODIS) and LCC (from CAMSiRA). Change is significant only for CAMSiRA (pvalue = 0.004), while for MODIS the pvalue is as high as 0.21. The shading indicates the standard deviation, which is spatial, being these averages over the whole area.

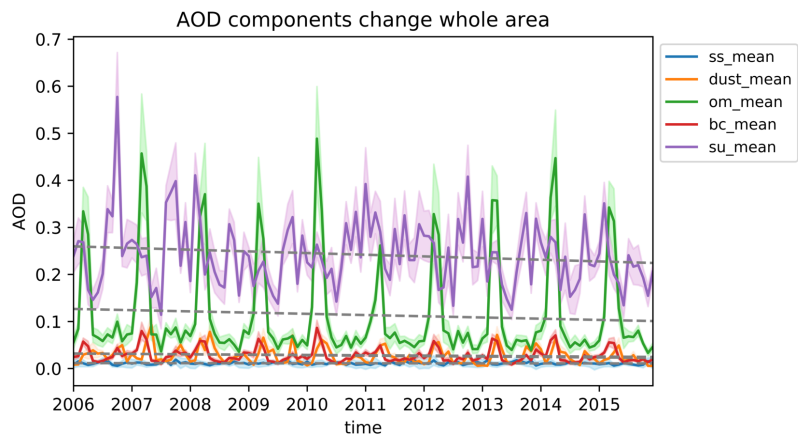


Figure 3: 10-years time series of monthly means, averaged over the whole area, of the 5 components of the AOD provided by CAMSiRA. The shading indicates the standard deviation. ss = seasalt; dust = dust; om = organic matter; bc = black carbon; su = sulphates.

ables available from CAMSiRA to study the modifications in the boundary layer conditions, which is the main purpose of this study.

Subsequently, the spatial variation of the changes in total AOD and LCC from CAMSiRA over the 10-years period was analysed (Figure 4). Results show that AOD decreases in the whole area, with a percentage change that varies from -5% to -21%. The strongest decreases are located over land and in particular in the North-West, while the smallest decreases are encountered in the coastal area and over sea, in particular in the gulf between the Leizhou peninsula and Vietnam.

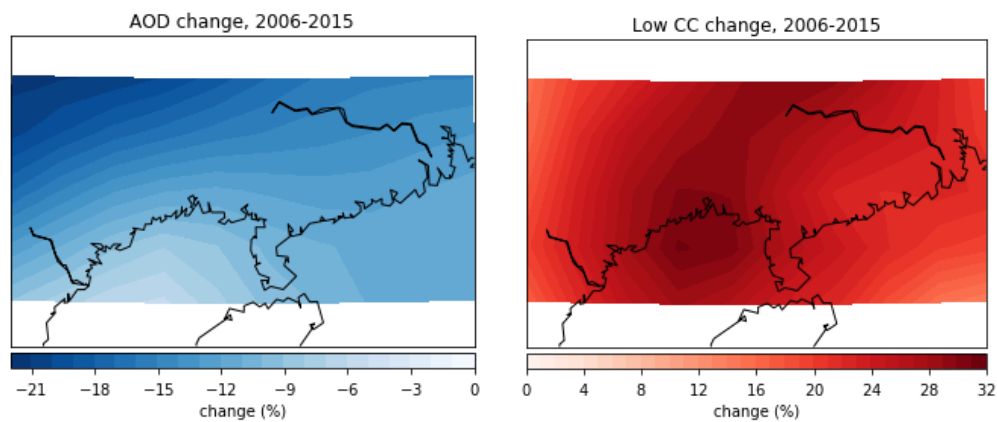


Figure 4: Spatial variation in the 10-years period percentage changes in AOD (left) and LCC (right). Data are from CAMSiRA.

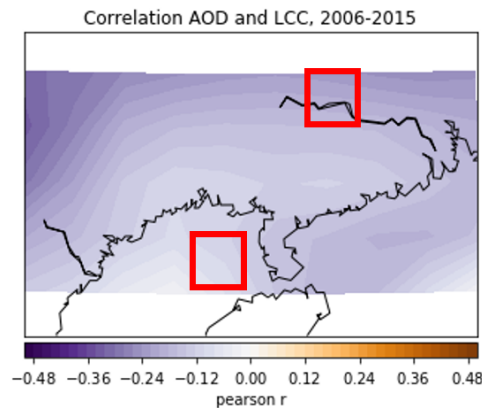


Figure 5: Correlation coefficient (Pearson r) between deseasonalized monthly means of AOD and LCC.

Instead, cloud cover increases in the whole area, ranging from +20% to +7%. The biggest increases in LCC are located between the gulf between the Leizhou peninsula and Vietnam and the North-East of the studied area,

while the lowest increases are found in the East over sea, and in the West, over land.

The correlation coefficient (Pearson's r) between AOD and LCC's de-seasonalized time series was calculated over the whole area and the outcome is shown in Figure 5. With an always negative correlation coefficient, the two variables show a weak anti-correlation over the whole studied area, which is however mostly above -0.3 and therefore not significant. The two variables are anti-correlated the most over the gulf between the Leizhou peninsula and Vietnam, while the Pearson's r approaches zero towards the edges of the studied area, apart from a stronger anti-correlation area in the South-East corner.

Although the anti-correlation between the two variables is weak, this analysis helped selecting the inland and coastal location for the conditional analysis. The locations are indicated by the two red squares in Figure 5.

The selected inland location is centred at 24.5°N and 111.5°E , where the correlation coefficient is -0.26. We chose this spot over the North-West corner, which has the largest negative correlation coefficient, because we also took into account the pattern in LWP changes shown by CLARA-A2 (Figure 1.b), and the variation in total cloud cover changes (Figure 6).

The selected coastal location is centred at 20.5°N and 109.5°E , where the correlation coefficient is about -0.07.

The changes in spatial variations of each of the five components of the total AOD, and their correlation with the LCC, can be found in Appendix.

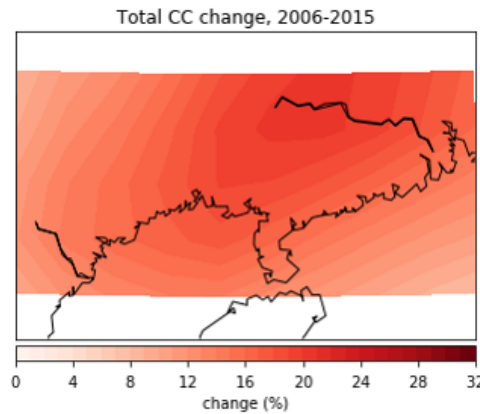


Figure 6: Spatial variation in the 10-years period percentage changes in total cloud cover. Data are from CAMSiRA.

3.1.1 Inland/coastal comparison

In this section the changes in the variables at the two selected locations will be compared, by means of their percentage changes and significance coefficients (pvalue, indicating significance when <0.05).

At the inland location, the deseasonalized AOD decreases by 16% and the increase in LCC is 29%. These changes are significant, showing pvalues of 0.004 and 0.005, respectively.

The variable which is directly affected by the increase in total cloud cover (20% at this location, Figure 6) is the short-wave incoming radiation, which shows a decrease of 10.7% (from 175 W m^{-2} to 155 W m^{-2} , with a pvalue of 0.003) (Figure 7a). The consequences of the decrease in SW_{in} are observed and lead to:

- A decrease in the net radiation (6.3%).
- A decrease in H (30.4%) (Figure 7c), an increase in LE (5.3%) (Figure 7d) and an increase in G (9.6%).
- A 2% decrease in the 2-meters temperature.
- A decrease in the ABL height by 12.7% (Figure 7b).

The change in H at the inland location is the most significant change observed in this analysis, with a pvalue of $7.9e^{-5}$. The change in LE, instead, is not significant. In particular, an increase in LE would not be expected, but rather a decrease, given the reduced amount of energy availability and the decrease in temperature.

For the coastal location, AOD decreases by 7.6% and LCC increases by 26.7%. We start again from the SW_{in} , which is decreasing at this location as well, but only by 2.9% (Figure 7a).

It is important to stress that although the difference in changes in LCC between the inland and coastal location is not so big (less than 3%), the larger difference between the changes in SW_{in} (around 8%) is to be related with the difference in total cloud cover at the two locations (which is around 9% indeed, see Figure 6). Although this study focuses on the boundary layer and therefore on low cloud cover, it is straightforward to say that SW_{in} and all the variables depending on it will be affected by the changes in total cloud cover and not only by the low one.

The consequences of a reduced decrease in SW_{in} , compared to the inland condition lead to the following changes:

- The net radiation remains quite stable, with a small increase of 0.3%.
- A decrease in H of 13.7% (Figure 7c), a decrease in LE of 6.2% (Figure 7d) and an increase in G (43.1%).

- A 1.2% decrease in the 2-meters temperature.
- A decrease in the ABL height of 6.1% (Figure 7b).

In this case changes are mostly not significant, which is consistent with the criteria used to select the coastal location. In fact, as stated in 2.2.4, this location should serve as a "control" case for comparison. Here, the small decrease in LE is expected, given the decrease in SW_{in} and surface temperature.

Given the changes in AOD, for the diurnal analysis (section 3.3) we will use 2006 as a more polluted year and 2015 as a less polluted year.

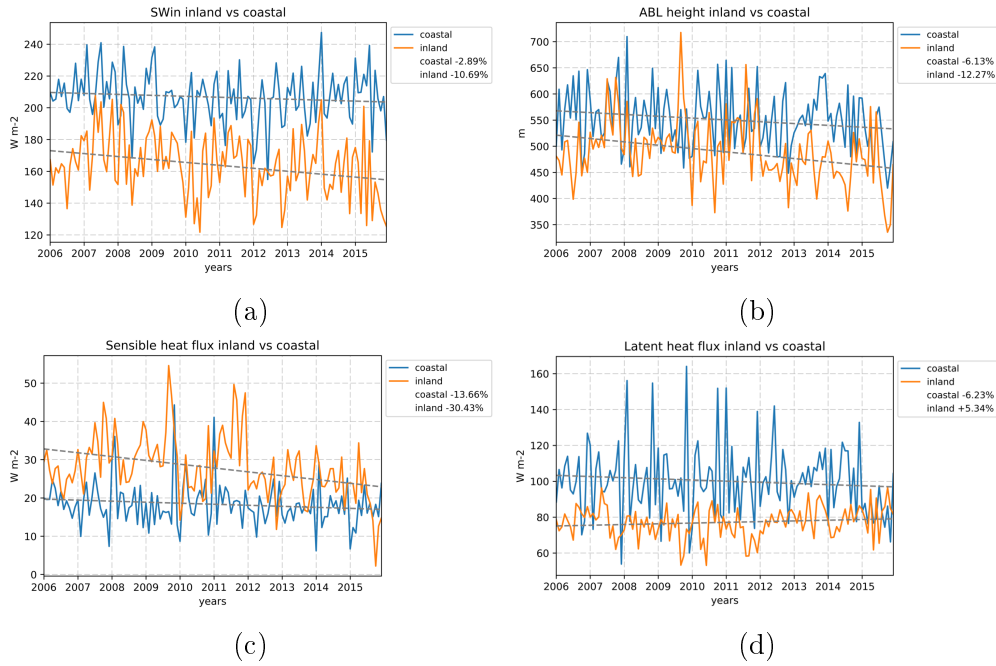


Figure 7: Time series of SW_{in} (a), ABL height (b), H (c), LE (d) in the 10-year period for the inland location (orange line) and the coastal location (blue line), along with the percentage changes. Changes are significant ($pvalue < 0.05$) in all cases, except for the coastal SW_{in} ($pvalue = 0.24$) and LE at both locations. Data are from CAMSiRA.

3.2 Monthly analysis

As explained in section 2.2.2, the monthly analysis is mostly aimed at the selection of one month to focus on for the daily analysis. Although it did not show the biggest anti-correlated changes in AOD and LCC (Table 1), the month of November was chosen, based mainly on the findings by Benas et al. (2017), which showed the large anti-correlation between changes in AOD and LCC in satellite data. Anyhow, the presence of big changes of the two variables in this month have been verified for CAMSiRA as well. The results of the monthly analysis revealed a decrease in AOD of 23.7% and an increase in LCC of 250.8% at the inland location (Figure 9). In Appendix, changes in AOD and LCC for all months can be found.

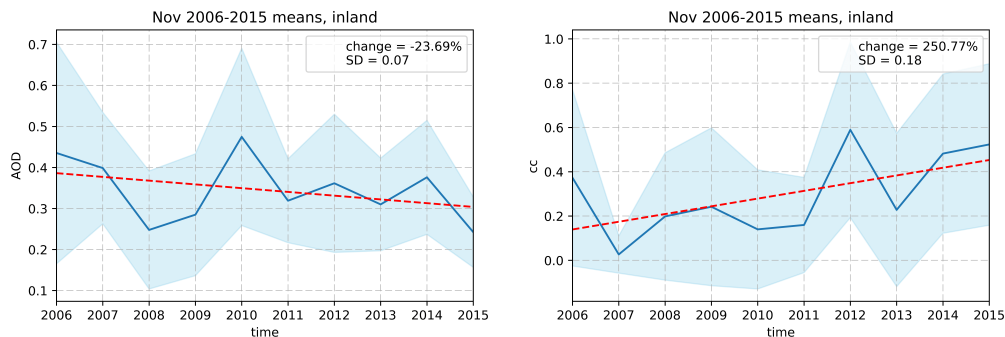


Figure 8: Time series of November monthly means from 2006 to 2015 for AOD (left) and LCC (right). Changes are relative to the inland location, since changes over the coast are (by choice) less pronounced and not used to establish the month to focus on for the diurnal analysis. Data are from CAMSiRA.

Table 1: Correlation coefficients (Pearson's r) between AOD and LCC for all months during the 10-years period 2006-2015.

Jan	Feb	Mar	Apr	May	Jun
-0.31	-0.59	-0.40	-0.08	-0.09	0.36
Jul	Aug	Sept	Oct	Nov	Dec
0.13	-0.28	-0.05	-0.63	-0.17	-0.24

3.3 Diurnal analysis

Given the results of the yearly and monthly analyses, the diurnal analysis is aimed at characterizing an average November day in 2006 and one in 2015, both at the inland and at the coastal location. To characterize this typical diurnal evolution of ABL variables, we studied the radiation budget, the surface energy budget and the evolution of the ABL height.

3.3.1 Radiation budget analysis

The average diurnal evolution of the components of the radiation budget in November 2006 and 2015 at both locations was computed and is shown in Figure 9. The time of the day is given in local time. Note that the value of a variable at a certain time is the average of 3 hours, due to the fact that fluxes are given as accumulated fields, as explained in 2.1.2.

Results showed that on an average November day at the inland location in 2006, when AOD was higher and cloud cover lower, the SW_{in} would peak at 12:00 at 490 W m^{-2} , and the SW_{out} at around 30 W m^{-2} . The thermal radiation shows, as it is expected, a less pronounced diurnal cycle, oscillating around $350\text{-}410 \text{ W m}^{-2}$, with the LW_{out} higher than LW_{in} . The net radiation peaks at 12:00 at 340 W m^{-2} .

On an average November day at the coastal location, also in 2006, the SW_{in} would peak at 12:00 at 600 W m^{-2} , and the SW_{out} at around 15 W m^{-2} . This makes sense since the cloud cover is higher over land than over sea. The thermal radiation shows even less diurnal changes than at the inland location, because of the different surface (sea), and oscillates between $390\text{-}420 \text{ W m}^{-2}$, with the LW_{out} higher than LW_{in} . The net radiation is much higher than in at the inland location, peaking at midday at 500 W m^{-2} .

In 2015 at the inland location, when the AOD has decreased by 23.7% and the increase in LCC is of 250.8% (changes relative to November only, Figure 8), the SW_{in} peak has decreased to 380 W m^{-2} and the SW_{out} peaks instead at 45 W m^{-2} . This is consistent with the results of the yearly analysis, showing that the SW_{in} decreases over the 10-year period, most likely directly due to the increase in cloud cover. The terrestrial radiation components have also decreased, ranging between $360\text{-}390 \text{ W m}^{-2}$, again with the LW_{out} higher than LW_{in} . The net radiation is therefore also lower, with a peak at 300 W m^{-2} .

In 2015 at the coastal location, the radiation fluxes have also decreased, but less than at the inland location. This is consistent with the results of the yearly analysis (3.1.1), which showed the coastal location to present the same kind of changes as the inland location, but with a smaller magnitude. This is, in turn, expected, given the difference in cloud cover prescribed with the selection of the two locations.

Indeed, the SW_{in} peaks at 620 W m^{-2} and the SW_{out} at 20 W m^{-2} . LW radiation components are mostly constant, with the LW_{in} at 395 W m^{-2} and the LW_{out} at 450 W m^{-2} . The net radiation reaches 454 W m^{-2} at midday.

To summarize, net radiation and the SW_{in} become lower in 2015 at both locations - if we take into account the variability indicated by the standard deviation. This feedback is observed more over land than at the

coast, consistently with the results of section 3.1.1. In general, the radiation budget on the coast is higher than the one over land. The standard deviation (shaded areas in Figure 9) is smaller at the coastal location than at the inland location. This can be related again with the difference in surface between the two locations: the lower heat capacity of land compared to water leads to bigger oscillations in the radiation components over land than over sea.

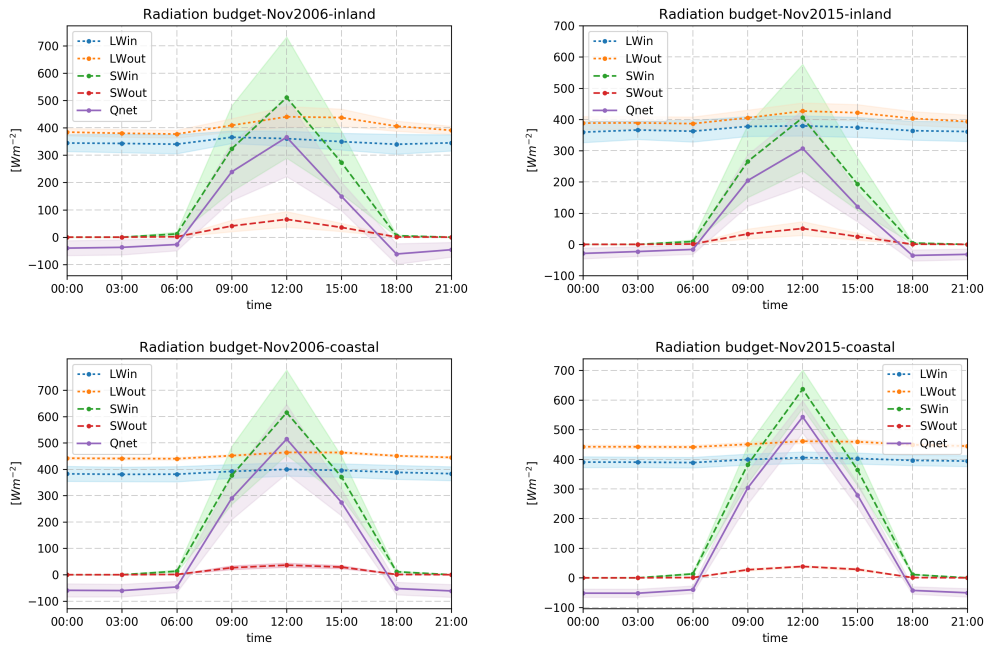


Figure 9: Radiation budgets of the four average November days, in 2006 and in 2015 for the inland and coastal locations. The shading indicates the standard deviation of the values. Time is in local time. Data are from CAMSIRA.

3.3.2 Surface energy balance analysis

Regarding the surface energy balance, the average diurnal evolution of the surface fluxes in the four conditions are shown in Figure 10.

On an average November day in 2006 at the inland location, the latent heat flux is the biggest component of the surface energy balance, peaking at 12:00 at around 150 W m^{-2} ; the sensible heat flux follows with a daily maximum of 135 W m^{-2} ; the ground heat flux is the smallest component and reaches 50 W m^{-2} . Net radiation, as already discussed, peaks at 340 W m^{-2} .

On an average November day in 2006 at the coastal location, the latent heat flux is higher than at the inland. This makes sense considering the bigger availability of energy, as discussed in the previous section, and the considerably higher availability of water. In this case, indeed, LE has its maximum at 240 W m^{-2} . H is the smallest component, with a peak of 20 W m^{-2} , and the rest is absorbed by the sea.

At the inland location, in 2015, LE is the biggest component with a peak of 180 W m^{-2} ; H is the second biggest component, with a daily maximum of 80 W m^{-2} ; G is the smallest component, with a peak of 40 W m^{-2} . As already seen, the net radiation has decreased.

At the coastal location, in 2015, the fluxes have undergone small changes, the most remarkable consisting of the increase by about 50 W m^{-2} of the energy absorbed by the sea. The net radiation shows an increase of about 25 W m^{-2} , consistent with the 10-year period time series for the coastal location, that indicated a slight increase of 0.3% (section 3.1.1).

We can summarize that the net radiation becomes lower in 2015 at both locations, but more at the inland than at the coastal one. In general, the net radiation at the coast reaches higher than over land. The biggest differences between the two locations consist in the magnitude of the standard deviation, as in 3.3.1, and in the entity of the ground heat flux. In fact, G is much higher during daytime and much more negative at night over the sea than at the coast, showing the larger amount of energy absorbed during the day and released at night by the water body.

Consistently with the results in 3.1.1, LE is increasing at the inland location while decreasing at the coastal location. The partitioning of the available energy into the various surface fluxes depends on surface characteristics like the availability of soil water, vegetation and other site-specific features (Betts et al., 2015), which are not available in this study.

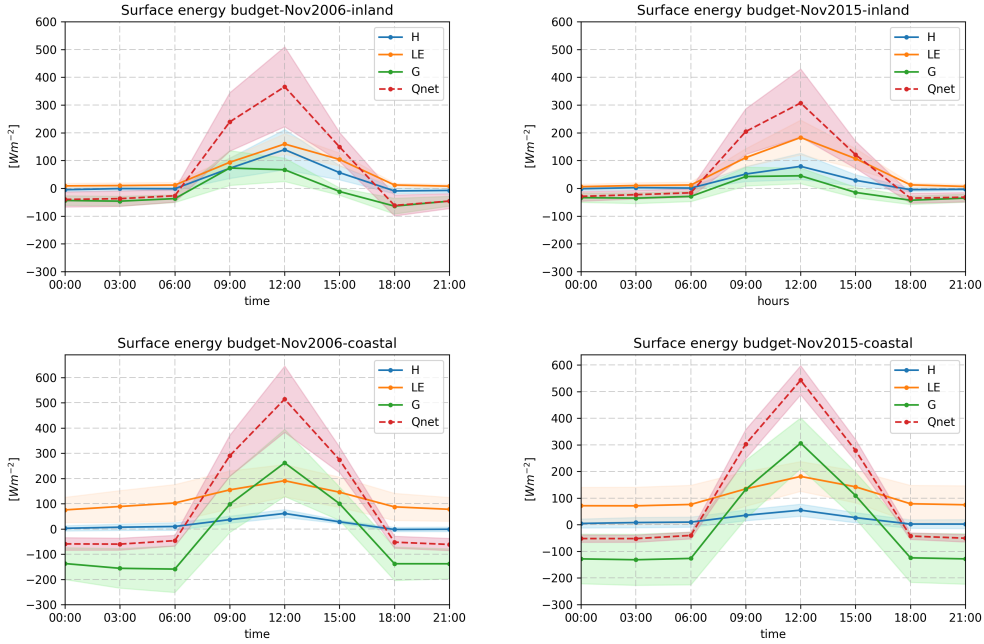


Figure 10: Surface energy balances of the four average November days, in 2006 and in 2015 for the inland and coastal locations. The shading indicates the standard deviation of the values. Time is in local time. Data are from CAMSiRA.

3.3.3 Potential temperature and specific humidity

The average November diurnal evolution of potential temperature and specific humidity has also been analysed in 2006 and 2015, and for the inland and coastal locations. Here we show the results for the lowest layer of the model (Figure 11).

The first thing that we observe is that for the inland, the potential temperature shows a more pronounced diurnal variation than over sea, and lower values. The first is probably due to the different heat capacity of the two surfaces, since land tends to heat up and cool down faster, leading to the more marked diurnal variation of potential temperature. The latter can be related with the larger energy availability over sea than over land seen in 3.3.1 and 3.3.2.

For 2006, the minimum θ is at night and is 287.5 K, while the maximum is reached between 12:00 and 15:00 with 294 K. In 2015, θ shows similar values at night (min: 288 K), but lower values by day, peaking at 292.5 K at 12:00. This is consistent with the 10-year decrease in the 2-meters temperature (3.1.1).

For the coastal location, differences are less pronounced, and so is the diurnal variation. Temperatures are in general higher: the minimum at night is reached at 296 K; the maximum is at 15:00 in 2006 (299.5 K) and between 12:00 and 15:00 in 2015 (298 K).

The specific humidity shows in all four cases a barely pronounced diurnal cycle, which is however more enhanced on the inland (where there is a slight increase during the day) than on the coast (where a decrease is noticed during the day compared to the night).

In 2006, on the inland, q is 0.010 kg kg^{-1} at night and kg kg^{-1} by day. In 2015, it is always around 0.008 kg/kg .

On the coast, in 2006, q oscillates around 0.014 kg kg^{-1} and around 0.015 kg kg^{-1} in 2015.

The values of the specific humidity are higher over the coast probably due to higher availability of water, and increase in 2015 at both locations most likely due to the decrease in ABL height (as seen in Figure 7b), which makes the water vapour more concentrated.

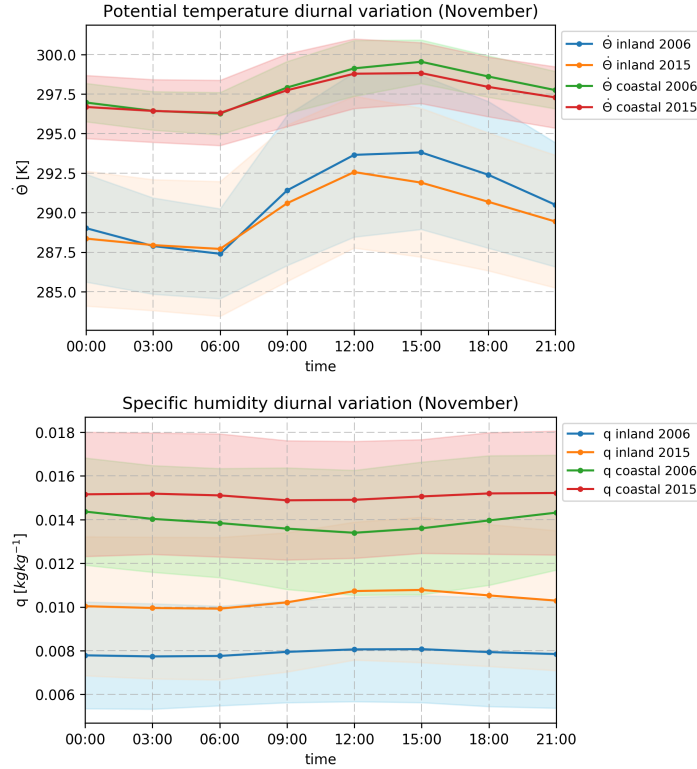


Figure 11: November average diurnal cycle at the lowest model level ($\sim 10 \text{ m}$ height) under the four conditional analyses (inland and coastal, in 2006 and 2015) of potential temperature (θ) (top) and specific humidity (q) (bottom).

Along with the diurnal cycles, the vertical profiles of θ and q have been analysed under the same conditions: in 2006, 2015 and for both inland and coastal locations, and the outcome is shown in Figure 12. Here we only compare the vertical profiles of the two variables at 14:00, while the vertical profiles of the whole day can be found in the Appendix (D).

Consistently with the diurnal evolution's analysis, the vertical profiles

of potential temperature at the inland location show a higher θ in 2006 than in 2015 (about 1 K higher) between the surface and ~ 890 hPa, where the two profiles converge. The same trend is observed on the coast, where the average difference between 2006 and 2015's profiles is less than 0.5 degrees. On the coast, the two profiles converge at around 925 hPa. In both cases, it is possible to notice the difference in ABL height (where the jump in the value of θ is located), which is lower in 2015. This is also consistent with the negative change in the ABL height observed during the yearly analysis (Figure 5b).

For the specific humidity, values are higher in 2015 than in 2006, both at the inland and on the coast. The average difference between the inland q is 0.003 kg/kg, while on the coast is about 0.0015 kg/kg. The reasons for the different magnitudes in changes are the the same as the ones illustrated above for the diurnal evolution of θ and q .

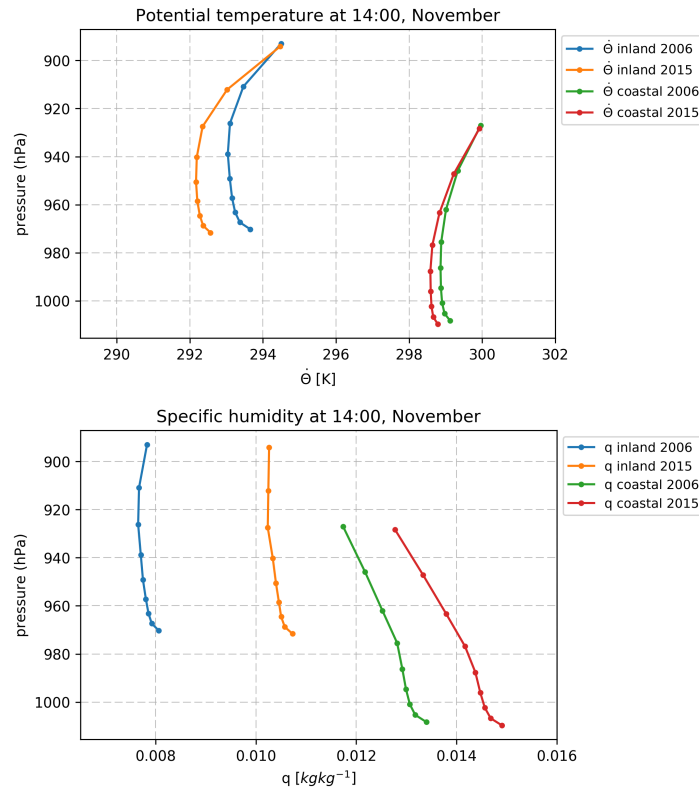


Figure 12: November average vertical profiles under the four conditional analyses (inland and coastal, in 2006 and 2015) of potential temperature(θ) (top) and specific humidity (q) (bottom).

4 Summary and Discussion

In this study we aimed to characterize the modifications in radiation, surface properties and boundary layer dynamics (ABL) over Southern China in the 10-year period 2006-2015, under conditions of increasing cloud cover and decreasing aerosol optical depth (AOD), while supporting recent remote sensing evidence of these changes (Benas et al., 2017).

For this purpose, the products of the Copernicus Atmosphere Monitoring Service interim Reanalysis (CAMSiRA) and the MODerate resolution Imaging Spectroradiometer (MODIS, used in the study by Benas et al. (2017)) have been compared and showed similar values and changes in AOD and low cloud cover (LCC, from CAMSiRA; liquid cloud fraction, LCF, from MODIS) in the 10-years period over the study area. They showed an average decrease of 17.7% (MODIS) and 13.5% (CAMSiRA) in AOD and an increase of 6.8% in LFC (MODIS) and 23.9% in LCC (CAMSiRA). The decreases in AOD are consistent with recent findings on reduction in biomass burning emissions in the study area (He et al., 2011).

The analysis of the spatial variation of the two variables showed that the largest changes in AOD and cloud cover were observed over land, similarly to the results by Benas et al. (2017). The largest anti-correlation between the two variables was also located over land - even though anti-correlation was weak over the whole area, as mentioned in section 3.1 (Yearly Analysis). However, the spatial analysis of the correlation coefficient does not allow to draw further conclusions on the relation between the two variables, and served mostly for the selection of an inland and a coastal locations to compare.

A decrease in SW_{in} was observed (10.7% over land, 2.9% on the coast), which is associated to the increase in total cloud cover (20% over land, 11% on the coast), although the reasons behind this outstanding increase in cloud cover were not investigated here. The decrease in SW_{in} is associated with a decrease in the net radiation (by 6.3% over land and 0.3% on the coast). The reduced energy availability in the ABL leads then to a decrease in the sensible heat flux which leads to a lower ABL height (by 12.2% over land and 6.1% on the coast). The changes in LE are less easily explained. They could be related to site-specific features, as mentioned in 3.3.2. They could also be related to the AOD, but different feedbacks are known between LE and AOD. For example, Li et al. (2017) found that aerosols cool the surface and reduce the LE, while Persad et al. (2017) describes suppression of LE under heating by absorbing aerosols.

In conclusion, all the changes observed could be related with the increase in cloud cover while the direct effect of aerosols on the surface and boundary layer dynamics could not be identified in this case study. This

suggests that clouds have a dominant effect on the changes in ABL conditions in Southern China during the study period, which could imply a dominance of cloudy-sky mechanisms for aerosols (section 2.2). Therefore, the SDE mechanism should not be excluded yet.

However, the lack of availability of vertical profiles of AOD in CAMSiRA does not allow to draw conclusions on possible effects of aerosols on clouds or on the surface variables. On the other hand, the components of the total AOD are made available and, as shown in section 3.1 (Yearly Analysis), sulphates form the main component, while the SDE effect is only applicable to absorbing aerosols (Johnson et al., 2004).

The month of November for the diurnal analysis was mainly chosen following the findings by Benas et al. (2017), which showed high correlation between changes in AOD and LCC, even though the presence of high changes of the two variables in this month have been verified for CAMSiRA as well (section 3.2).

Radiation and surface energy budgets of the four average November days were analysed (in 2006 and in 2015 for both inland and coastal locations). It was observed that in both cases the radiation and surface energy balances become lower in 2015, but the changes are more pronounced at the inland location than at the coastal one due to the bigger changes in cloud cover there (section 3.3). These findings were consistent with the results of section 3.1.

Similar changes were observed when comparing the diurnal evolutions and the vertical profiles of potential temperature and specific moisture under the same four conditions (section 3.4). In fact, the potential temperature decreased in 2015 at both locations, but by a larger amount over land (~ 2 K) than on the coast (< 1 K). This is probably due not only to the different magnitudes in cloud cover changes, but also to the different surface (land versus sea), and in particular to the different heat capacity of these. Instead, the specific moisture increased at both locations after 10 years, but the difference is larger over land ($0,0025 \text{ kg kg}^{-1}$ against $0,0015 \text{ kg kg}^{-1}$ on the coast). This result is probably also due to the different surface, given the larger availability of water at the coastal location.

It is acknowledged that the difference in heat capacity between land and sea might play a significant role in driving the evolution of the studied variables in the ABL, as discussed in 3.3.1, 3.3.2 and 3.3.4. However, the same kind of changes were observed over land and over sea, although with different magnitudes. This suggests that the difference in cloud cover is still the main driver of the 10-years period changes.

Another point worth mentioning is that the output of CAMSiRA has not been validated with observations in this study, apart from the comparison with MODIS. However, AOD from MODIS is already assimilated by

the model CAMSiRA (Flemming et al., 2017).

The results of this study will serve in a further phase of this research, as an input in a boundary layer model (CLASS, de Arellano et al. (2015)), which will be used to gain more insights over the role of aerosols in the case study, and the partitioning of the radiation in the ABL. This should help coping with limitations such as the coarse temporal resolution of CAM-SiRA - relative to a day - which did not allow to investigate ABL dynamics processes in detail, and the already mentioned constraint given by the lack of AOD vertical profiles.

References

- Anenberg, S. C., L. W. Horowitz, D. Q. Tong, and J. J. West (2010). An estimate of the global burden of anthropogenic ozone and fine particulate matter on premature human mortality using atmospheric modeling. *Environmental health perspectives* 118(9), 1189.
- Barbaro, E., J. V.-G. Arellano, H. G. Ouwersloot, J. S. Schröter, D. P. Donovan, and M. C. Krol (2014). Aerosols in the convective boundary layer: Shortwave radiation effects on the coupled land-atmosphere system. *Journal of Geophysical Research: Atmospheres* 119(10), 5845–5863.
- Benas, N., J. F. Meirink, K. G. Karlsson, M. Stengel, and P. Stammes (2017). Observational evidence of the aerosol semi-direct effect in south china from 2006 to 2015, in preparation.
- Betts, A. K., R. Desjardins, A. Beljaars, and A. Tawfik (2015). Observational study of land-surface-cloud-atmosphere coupling on daily timescales. *Frontiers in Earth Science* 3, 13.
- Boucher, O. (2015). *Atmospheric Aerosols*. Springer Netherlands.
- de Arellano, J. V.-G., C. C. Van Heerwaarden, B. J. Van Stratum, and K. Van Den Dries (2015). *Atmospheric boundary layer: Integrating air chemistry and land interactions*. Cambridge University Press.
- ECMWF (2017a). ECMWF 20 years of 4d-var: better forecasts through a better use of observations.
- ECMWF (2017b). ECMWF camsira, the cams interim reanalysis.
- ECMWF (2017c). ECMWF mars content.
- ECMWF (2017d). ECMWF what are the changes between the cams reanalysis and the macc and cams interim reanalyses?
- Flemming, J., A. Benedetti, A. Inness, R. J. Engelen, L. Jones, V. Huijnen, S. Remy, M. Parrington, M. Suttie, A. Bozzo, et al. (2017). The cams interim reanalysis of carbon monoxide, ozone and aerosol for 2003-2015. *Atmospheric Chemistry and Physics* 17(3), 1945.
- He, M., J. Zheng, S. Yin, and Y. Zhang (2011). Trends, temporal and spatial characteristics, and uncertainties in biomass burning emissions in the pearl river delta, china. *Atmospheric environment* 45(24), 4051–4059.
- Jacob, D. (1999). *Introduction to atmospheric chemistry*. Princeton University Press.

- Janhäll, S., K. F. G. Olofson, P. U. Andersson, J. B. Pettersson, and M. Hallquist (2006). Evolution of the urban aerosol during winter temperature inversion episodes. *Atmospheric Environment* 40(28), 5355–5366.
- Jethva, H., O. Torres, and C. Ahn (2016). A ten-year global record of absorbing aerosols above clouds from omi’s near-uv observations. In *Remote Sensing of the Atmosphere, Clouds, and Precipitation VI*, Volume 9876, pp. 98761A. International Society for Optics and Photonics.
- Johnson, B., K. Shine, and P. Forster (2004). The semi-direct aerosol effect: Impact of absorbing aerosols on marine stratocumulus. *Quarterly Journal of the Royal Meteorological Society* 130(599), 1407–1422.
- Karlsson, K.-G., K. Anttila, J. Trentmann, M. Stengel, J. F. Meirink, A. Devasthale, T. Hanschmann, S. Kothe, E. Jääskeläinen, J. Sedlar, et al. (2017). Clara-a2: the second edition of the cm saf cloud and radiation data record from 34 years of global avhrr data. *Atmospheric Chemistry and Physics* 17(9), 5809.
- Koch, D. and A. Del Genio (2010). Black carbon semi-direct effects on cloud cover: review and synthesis. *Atmospheric Chemistry and Physics* 10(16), 7685–7696.
- Levy, R., S. Mattoo, L. Munchak, L. Remer, A. Sayer, F. Patadia, and N. Hsu (2013). The collection 6 modis aerosol products over land and ocean. *Atmospheric Measurement Techniques* 6(11), 2989.
- Li, Z., J. Guo, A. Ding, H. Liao, J. Liu, Y. Sun, T. Wang, H. Xue, H. Zhang, and B. Zhu (2017). Aerosol and boundary-layer interactions and impact on air quality. *National Science Review*.
- Persad, G. G., D. J. Paynter, Y. Ming, and V. Ramaswamy (2017). Competing atmospheric and surface-driven impacts of absorbing aerosols on the east asian summertime climate. *Journal of Climate* 30(22), 8929–8949.
- Platnick, S., K. G. Meyer, M. D. King, G. Wind, N. Amarasinghe, B. Marchant, G. T. Arnold, Z. Zhang, P. A. Hubanks, R. E. Holz, et al. (2017). The modis cloud optical and microphysical products: Collection 6 updates and examples from terra and aqua. *IEEE Transactions on Geoscience and Remote Sensing* 55(1), 502–525.
- von Engel, A. and J. Teixeira (2013). A planetary boundary layer height climatology derived from ecmwf reanalysis data. *Journal of Climate* 26(17), 6575–6590.

- White, P. W. (2000). *IFS Documentation: Part III: Dynamics and Numerical Procedures (CY21R4)*. European Centre for Medium-Range Weather Forecasts.
- Yang, Y., J. Wang, S. Gong, X. Zhang, H. Wang, Y. Wang, J. Wang, D. Li, and J. Guo (2016). Plam—a meteorological pollution index for air quality and its applications in fog-haze forecasts in north china. *Atmospheric Chemistry and Physics* 16(3), 1353–1364.
- Zhao, S., J. Li, and C. Sun (2016). Decadal variability in the occurrence of wintertime haze in central eastern china tied to the pacific decadal oscillation. *Scientific reports* 6, 27424.

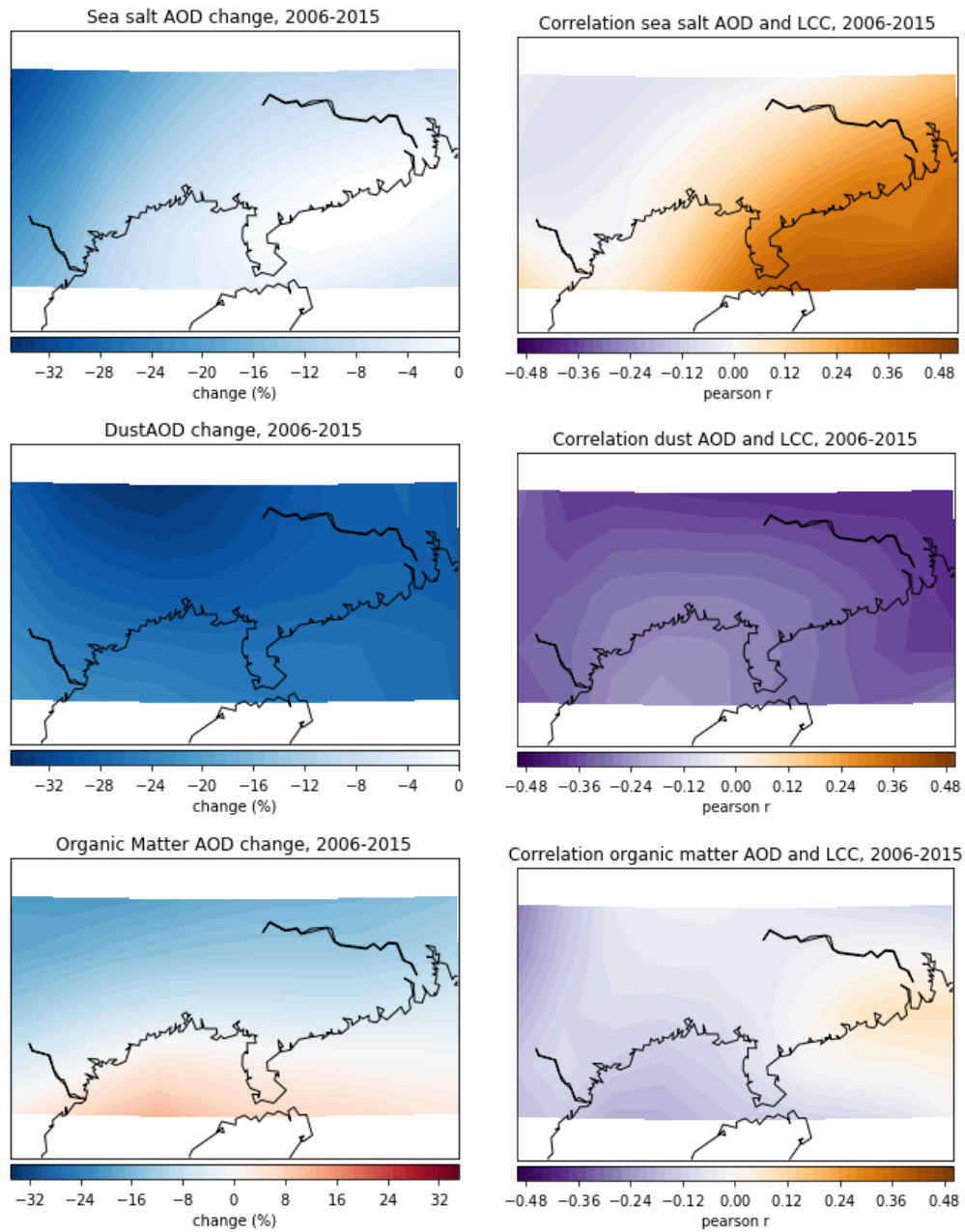
A Model levels (CAMSiRA)

In CAMSiRA, to represent the vertical variation of the variables, the atmosphere is divided into 60 layers. These layers are defined by the pressure (in hPa) at the interface between them (called ‘half-levels’), and the pressures are given by:

$$P_{k+1/2} = a_{k+1/2} + b_{k+1/2} * p_s \quad (7)$$

Where $0 \leq k \leq 60$, the two constants $a_{k+1/2}$ and $b_{k+1/2}$ are given for each model level and p_s is the surface pressure (in hPa), given on a pixel basis along with the model level parameters. In this way, it is possible to reconstruct the ‘full-level’ pressure for each level - more precisely, in the middle of the layer (White, 2000).

B AOD components: spatial changes and correlation with LCC



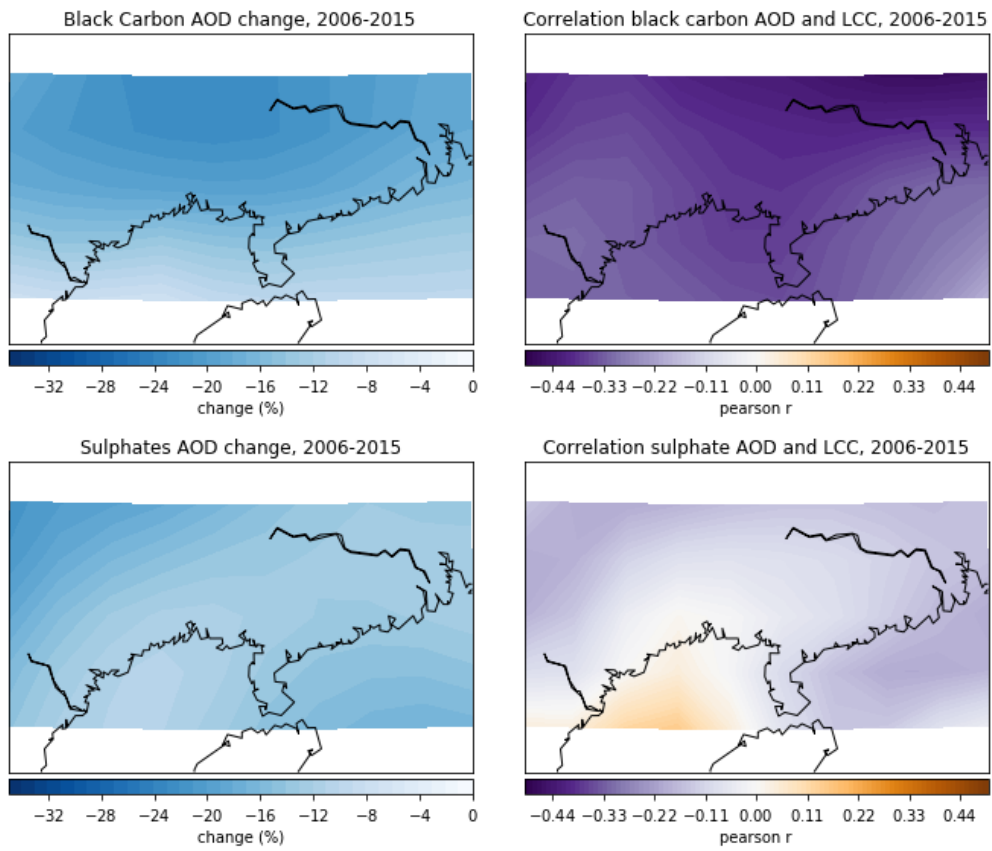
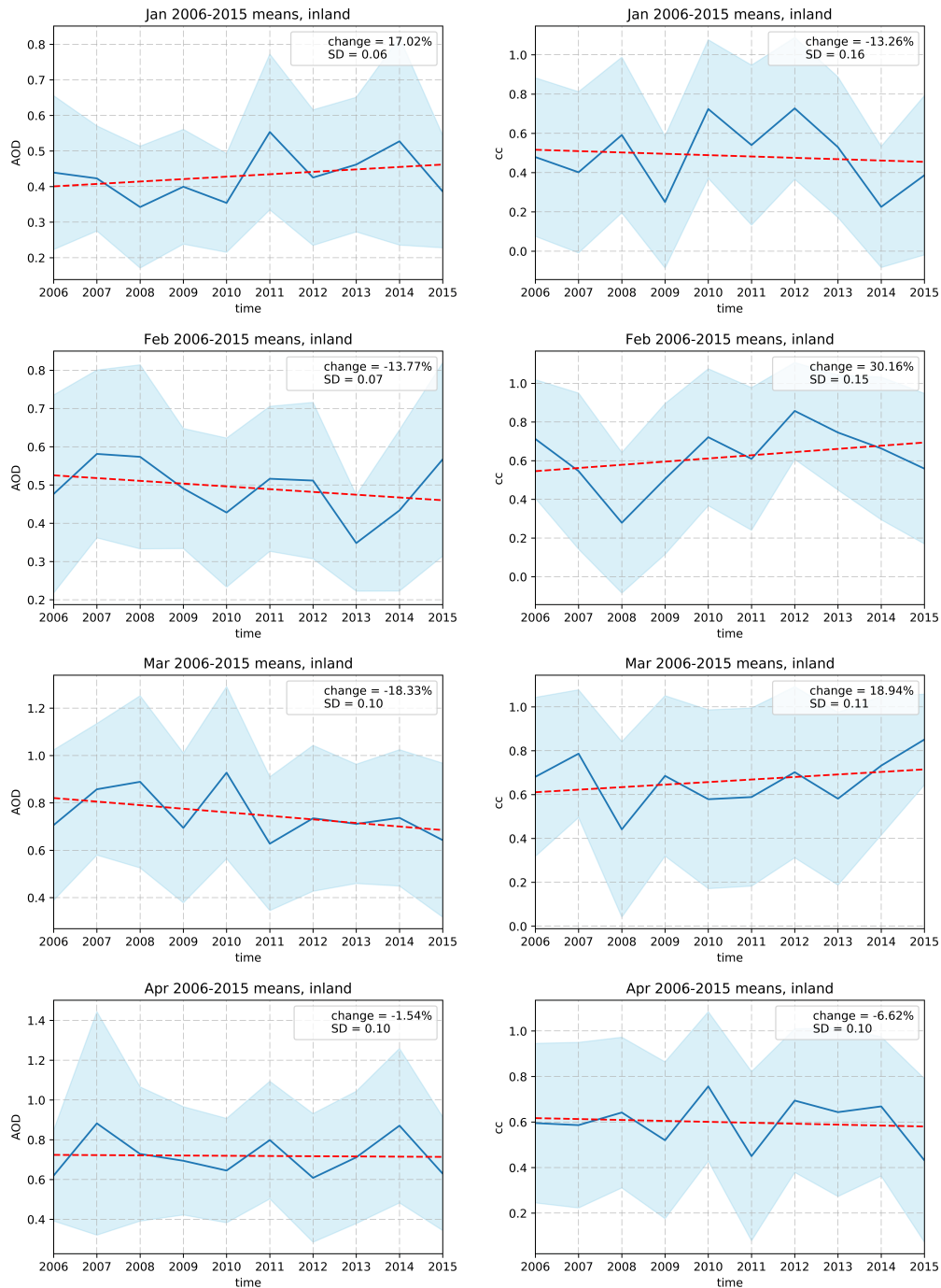
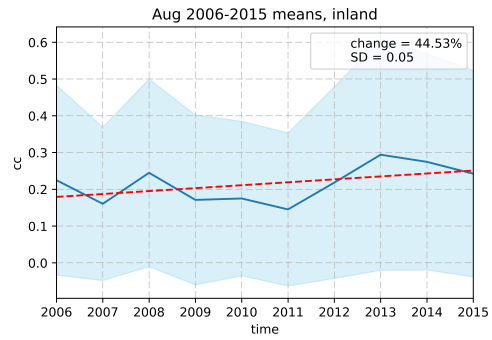
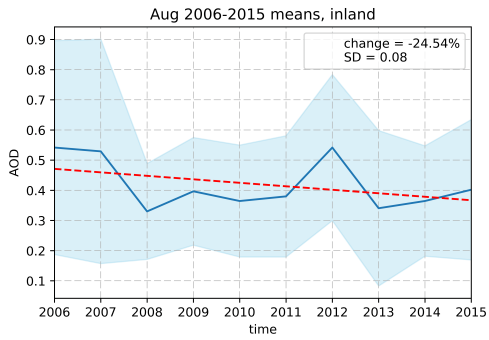
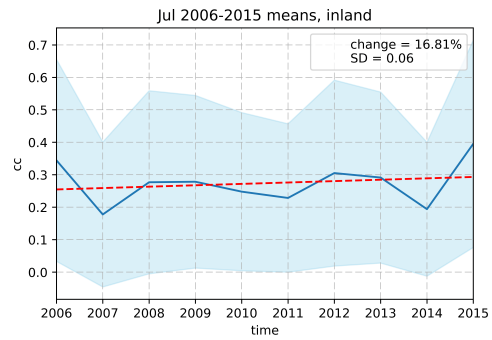
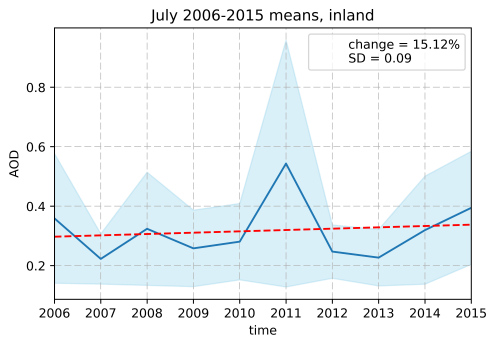
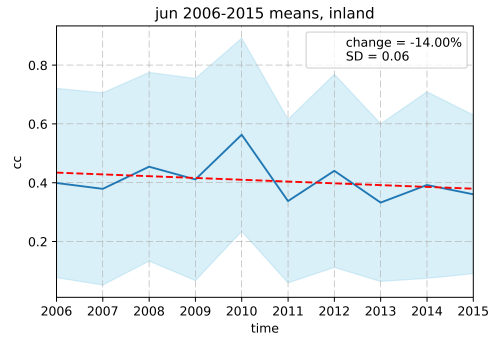
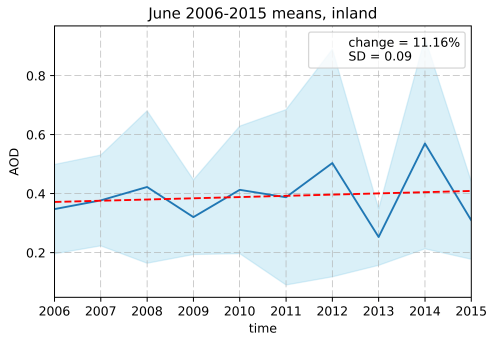
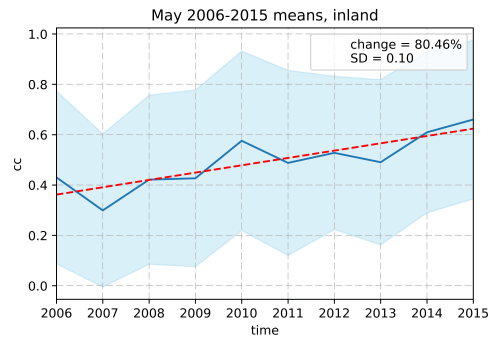
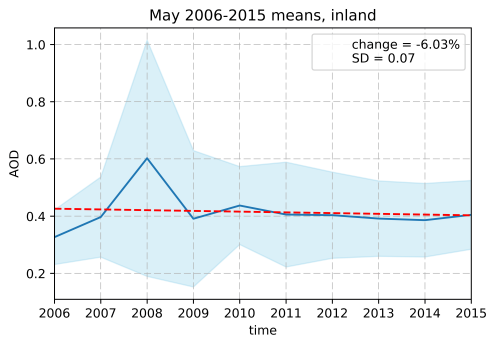


Figure 13: Spatial variation of changes in each of the five components of AOD (on the left) and correlation coefficient with LCC (Figure 4, right)

C Changes in AOD and LCC for all months





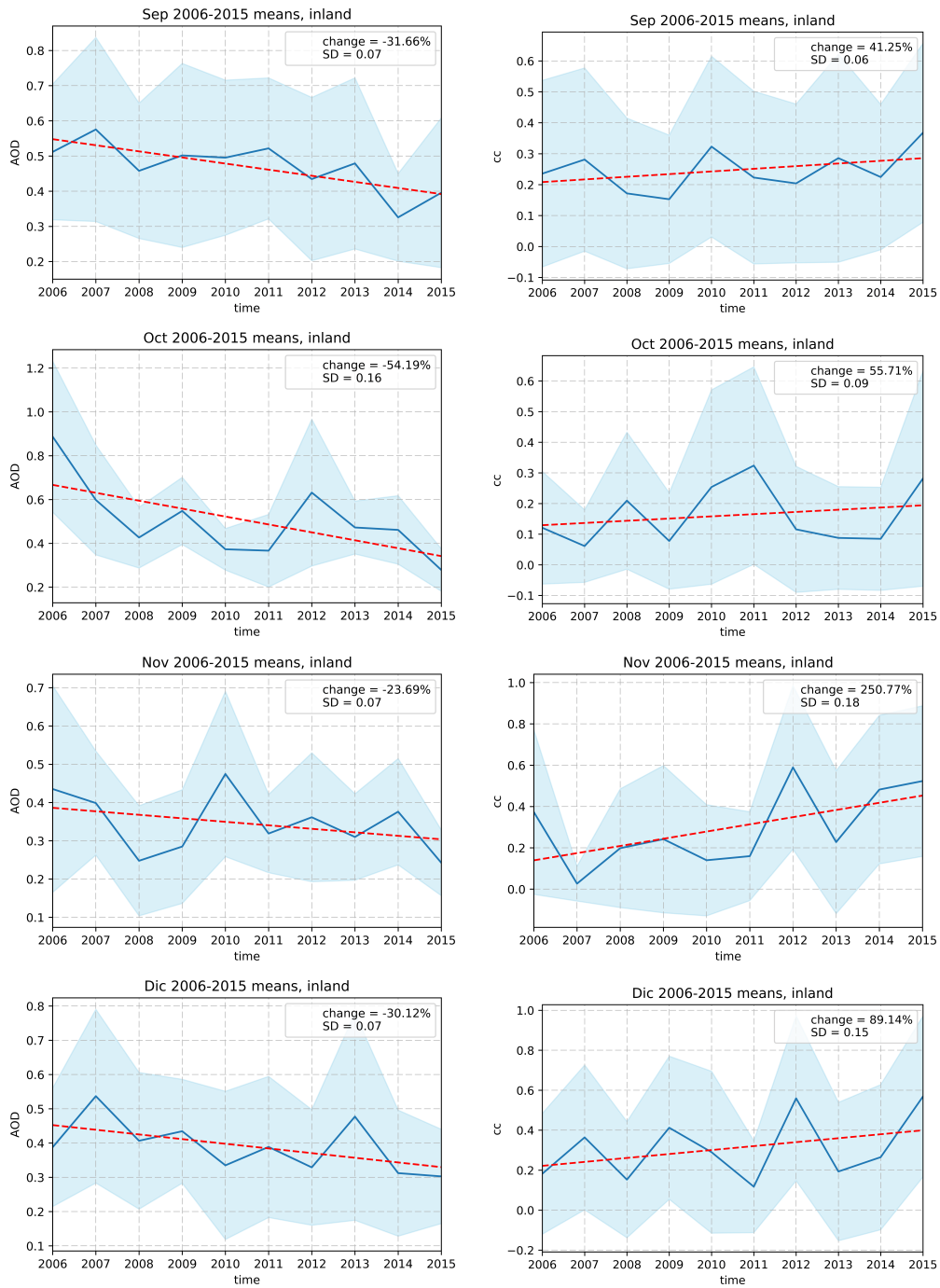


Figure 14: Changes in AOD and LCC for all months.

D Vertical profiles

D.1 Potential temperature

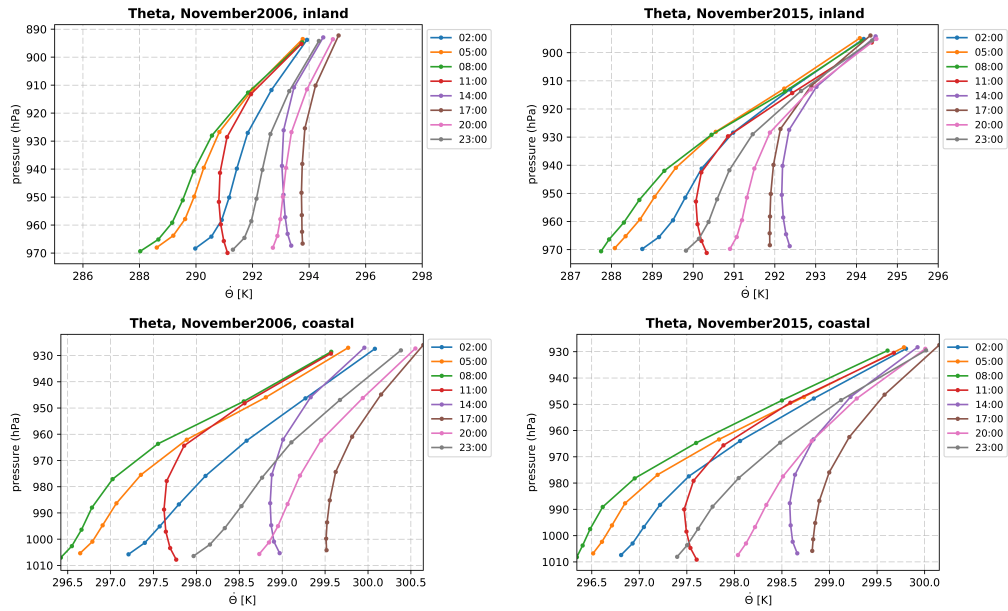


Figure 15: Vertical profiles of potential temperature on an average November day in 2006 and 2015, at the inland and coastal locations.

D.2 Specific humidity

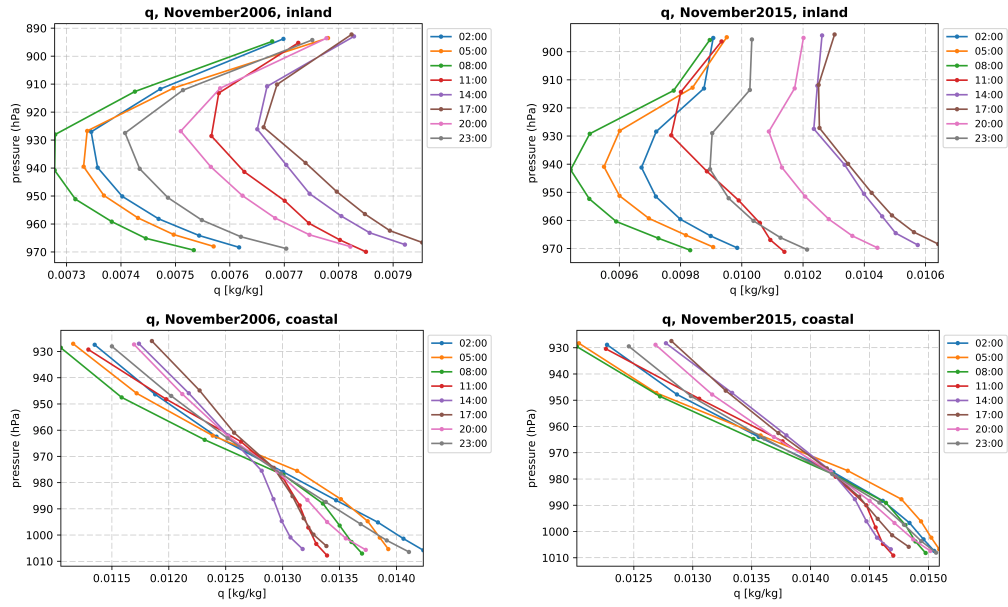


Figure 16: Vertical profiles of specific humidity on an average November day in 2006 and 2015, at the inland and coastal locations.